A back-projection approach to coded aperture imaging for SPECT applications

A. Costantino, A. Bird, James Schuffham, Matthew Guy

A. Costantino, A. J. Bird, James Schuffham, Matthew Guy, "A back-projection approach to coded aperture imaging for SPECT applications," Proc. SPIE 12031, Medical Imaging 2022: Physics of Medical Imaging, 1203139 (4 April 2022); doi: 10.1117/12.2610979

SPIE.

Event: SPIE Medical Imaging, 2022, San Diego, California, United States

A back-projection approach to coded aperture imaging for SPECT applications

A. Costantino[a], A. J. Bird[a], J. Scuffham[b], and M. Guy[c]

[a]Physics and Astronomy, University of Southampton
[b]Nuclear Medicine Physics, Royal Surrey County Hospital
[c]University Hospital Southampton NHS Foundation Trust

ABSTRACT

This work applies a back-projection approach to the reconstruction of images obtained with a 3D near-field coded aperture camera, a method derived from that used to analyse astronomical data collected by the INTEGRAL/IBIS instrument.[1] The method used in this paper is a form of deconvolution that updates the image as the camera or the object under observation is moving, and as such could be applied to dynamic studies or as a real-time surgical probe. Multi-isotope parathyroid imaging has been identified as one of the optimal applications of this technique, where high sensitivity and high energy resolution would permit the differentiation between thyroid and parathyroid tissues on the surgical table, and aid in different types of thyroid surgery. The back-projection technique is combined with a 3D version of the iterative CLEAN algorithm, which reduces the effect of the systematic noise intrinsic to imaging with a non-perfect aperture.

Keywords: Gamma-ray imaging, SPECT, coded mask, coded aperture, back-projection.

1. INTRODUCTION

The precise measurement of radiation distribution is a challenge that often arises in medical imaging. Single Photon Emission Computed Tomography (SPECT) typically uses multiple views of the body via different kinds of collimators to form images of organs in search for tissue abnormalities. Collimators are usually characterised by a 1% to 0.1% throughput, which results in a low count efficiency in the system. Since its development for gamma-ray astronomy, several attempts have been made to apply coded aperture imaging to the medical field[2–4] and significant progress has been made to adapt the technology to near-field imaging. Coded apertures are modulating patterns of open and closed "pixels" made of radiation absorbing materials, typically tungsten or lead. The coded aperture (or mask) is placed in front of a position-sensitive detector. When a gamma-ray source is observed, the map of detector counts, called the shadowgram, represents the shadow of the mask pattern onto the detector plane. An image can be deconvolved from the shadowgram using different techniques.[5–7]

2. METHODS

2.1 3D BACK-Projection

The reconstruction of an image through back-projection is performed by tracing each detected photon to all the positions in the field of view (FOV) from where it could have originated. The reconstruction algorithm uses pre-calculated projections in the form of 3D matrices that represent the single-pixel visibility of the field of view. For each detector pixel, a single pixel projection matrix G is computed by assigning a value to each voxel in the FOV :

$$G_{i,j,k}(l,m) = \begin{cases} 1, & \text{if voxel } i,j,k \text{ is visible from detector pixel (l,m)} \\ -1 & \text{if if voxel } i,j,k \text{ is obscured from detector pixel (l,m)} \end{cases} . \quad (1)$$

The value of G represent whether the voxel i,j,k in the deconvolved image can be seen by the detector pixel through an opening in the coded mask. The single pixel projections are computed with the aid of the NVIDIA

Send correspondence to A. Costantino
E-mail: a.costantino@soton.ac.uk

Medical Imaging 2022: Physics of Medical Imaging, edited by Wei Zhao, Lifeng Yu, Proc. of SPIE
Vol. 12031, 1203139 · © 2022 SPIE · 1605-7422 · doi: 10.1117/12.2610979

CUDA toolkit,[8] implemented in a code written with the Python open-source JIT compiler Numba.[9] The raw image of a radiation source is formed by adding together the matrices corresponding to each detector pixel, weighted by the number of counts c in the detector pixel itself, according to the equation

$$I_{i,j,k} = \sum_{l,m} G_{i,j,k} c_{l,m}. \tag{2}$$

2.1.1 Normalisation of single pixel projections

Single pixel back-projection matrices have the same role as the array G used in the 2D deconvolution process of coded mask images[5] and need to be appropriately normalised in order to obtain optimal background characteristics in the final image. Normalisation of the single pixel projections is called balancing and enables an image with flat background in the absence of sources. The appropriate balancing array to use is

$$B_{i,j,k} = \frac{n^{+}_{i,j,k}}{n^{-}_{i,j,k}}, \tag{3}$$

where $n^{+}_{i,j,k}$ is the number of detector pixels that can see the position of the voxel i,j,k through an opening in the mask, while $n^{-}_{i,j,k}$ is the number of detector pixels that can not see voxel i,j,k because the closed elements of the mask are blocking its view.[10] The value B is a property of the position in the field of view that depends on the geometry of the system and represents the local transparency of the mask, or the transparency of the sub-portion of the mask projected on the detector plane by a source in that position. The visibility matrix for each detector pixel is then constructed as follows:

$$G_{i,j,k}(l,m) = \begin{cases} 1, & \text{if voxel i j k is visible from detector pixel } (l,m) \\ -B_{i,j,k} & \text{if voxel i j k is obscured from detector pixel } (l,m) \end{cases}. \tag{4}$$

The image is obtained through the addition of these matrices, according to the following formula:

$$I_{i,j,k} = \sum_{l,m} G_{i,j,k} c_{l,m}, \tag{5}$$

where i, j, k represent the voxels of the final image I, G is the 3D single pixel back-projection and c is the number of counts in each detector pixel identified by l,m. The similarities between 5 and the 2D deconvolution formula[5] are evident, with the main difference that the shift of the deconvolution array is pre-computed in the single pixel projections. This allows for a photon-by-photon reconstruction approach, useful for dynamic or real time applications.

2.2 The 3D CLEAN Algorithm

The raw image obtained with back projection is characterized by background structures originated from the deconvolution process (coding noise). The CLEAN algorithm acts on the raw image resulting from the back-projection algorithm and produces a cleaned image, where the coding noise is reduced or completely eliminated. CLEAN is a family of algorithms devised by J.A. Högbom,[11] which are used in radio astronomy to process interferometry maps and reduce or eliminate sidelobes created by the reconstruction process. The known response of the instrument is used to identify and remove these artifacts in the final maps. This cleaning technique is based on two assumptions: any source in the field of FOV can be described as composed of a certain number of point sources, for which the PSF of the imaging instrument is known, and the position of the voxel with highest intensity in the image is part of the source. CLEAN is implemented through the following steps:

- The inputs of CLEAN are the raw image and a cleaned image, the latter is initially defined as an empty 3D array.
- Find the voxel with highest value I_{max} and calculate its coordinates in the FOV .

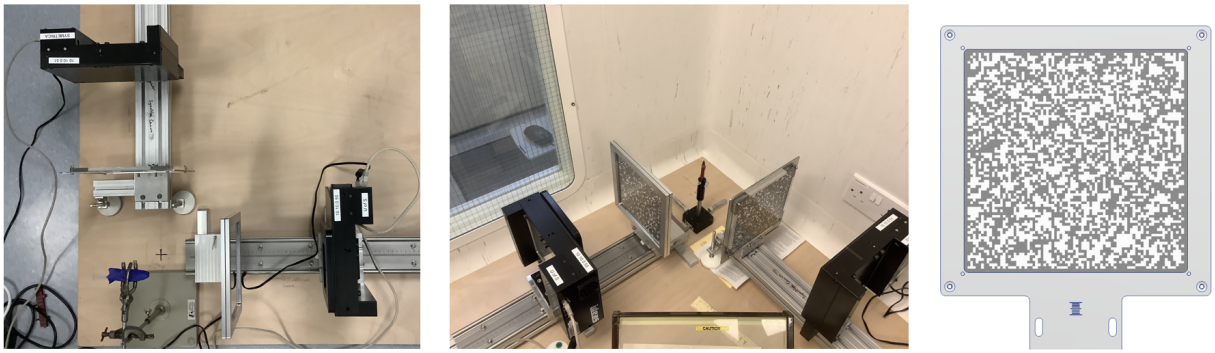

(a) (b) (c)

Figure 1: (a) and (b): Pictures of the imaging system during the experiments The two detectors in their black casings and the coded masks are fixed on two metal rails placed at a 90 degree angle. The source is placed where the axes of the two cameras meet, which is the centre of the FOV. (c) A drawing of the coded mask with the chosen pattern in its supporting frame.

- Compute the PSF of the instrument for a point source in the position of the voxel of highest intensity, which includes instrumental artefacts.
- Subtract the PSF from the raw image after normalising it to gI_{max}, where g is known as *loop gain* and is empirically set between 1% and 25%.[12]
- Add to the cleaned image the ideal component of the PSF.

The process is repeated iteratively until the source and the coding noise are completely subtracted from the raw image and I_{max} reaches the statistical noise. In the final step of the process, the residual noise in the raw image is added back to the sum of the cleaned components. In practice it is difficult to identify a single stopping criterion that will produce quality images of different types of sources, but different indicators can be used.

2.3 The Imaging System

Figure 1 shows the imaging system used for this study, composed of two cameras positioned at a 90 degree angle. A single coded mask camera provides lines of response through the field of view that are spread over a relatively narrow range of angles. As a result, although a single camera does produce a 3D image, the resolution along the camera's axis can be up to an order of magnitude lower that the lateral resolution. The axial resolution can be improved by using two cameras, each observing the source from a different angle, in a stereoscopic observation. For the system in figure 1, each camera has a 5 mm to 6 mm spatial resolution in the planes parallel to the detector, but the resolution along the camera axis is significantly worse (up to 120 mm). The combination of images from both heads produces a 3D image with an optimised lateral resolution along the axes of both cameras with a single view of the target. It should be noted that due to the geometry of the system, the lateral resolution is not constant, but varies across the field of view with the distance to each of the cameras.

The imaging system designed for this work consists of two IDEAS CZT gamma cameras, each composed of an array of 48×48 pixels, arranged in 3×3 modules of 16×16 pixels each $1.6 \times 1.6 \times 5$ mm. The camera is in its low energy configuration, which is recommended to be used for detection of gamma-rays in the range 0-350 keV. For the purpose of these experiments the detector on the left in figure 1 is referred to as detector 1, the one on the right is referred to as detector 2. Both detectors are placed at a distance of 210mm from each coded mask. This configuration has a nominal FOV of $21 \times 21 \times 21$ cm^3.

The mask was designed by taking a randomised pattern with 50% transparency and manually editing it so that every opaque pixel is connected to the rest of the mask by at lest one corner. The mask design is shown on the right in figure 1. The coded mask used to assemble the camera is made of a 2 mm thick layer of lead, which absorbs 99.5% of 140 keV photons. The lead was machined to obtain an 80×80 pattern of 2.2×2.2 mm^2 pixels.

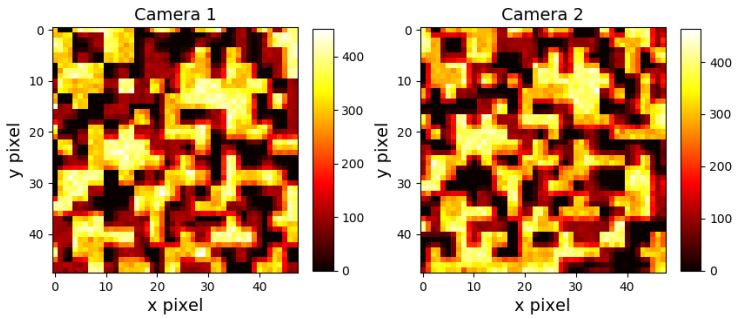

Figure 2: Dual head shadowgrams for two sources of different brightness.

3. SIMULATIONS

Before the assembly of the imaging system, simulations were run in order to assess the performance of the reconstruction algorithm. This simulations involved single and multiple point-like sources in the field of view.

3.1 Simulated data

The shadow projected on the detector plane for a specific source position is calculated and is used to simulate a shadowgram. A number of counts is assigned to each illuminated detector pixel following a Poisson distribution. At this stage second-order physical effects such as the transmission of the lead in the aperture plane or the effects of the source distance on the detector flux are not taken into consideration. Figure 2 shows the simulated shadowgrams in each of the detectors. The shadowgrams are generated by two point sources, A and B. The sources are positioned at (30 mm, 30 mm, 30 mm) and (−30 mm, −30 mm, −30 mm), where (0 mm, 0 mm, 0 mm) is the centre of the FOV. The average count rate on both detectors is 300 counts for source A and 100 counts for source B.

3.2 Results

For each shadowgram a raw image was computed using back-projection and then processed with CLEAN. A comparison between the raw image and the processed image is shown in figure 3. In the raw image source B is hard to identify among the decoding artifacts created by the brighter source A in the reconstruction process. By iteratively subtracting the ideal camera PSF from the raw image, CLEAN identifies and subtracts these components, returning an improved signal to noise ratio. The relative intensity of the sources is also correctly reconstructed, as shown in table 1.

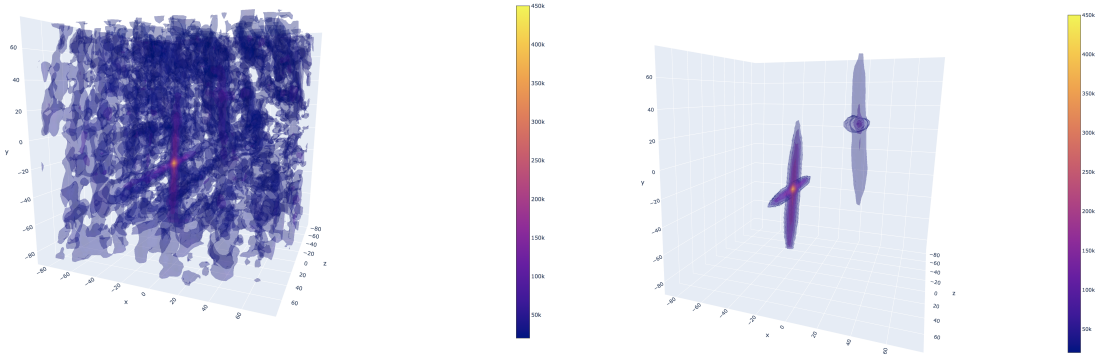

Figure 3: Left: Raw dual-head image of sources A and B. Right: Dual-head image of sources A and B processed with CLEAN.

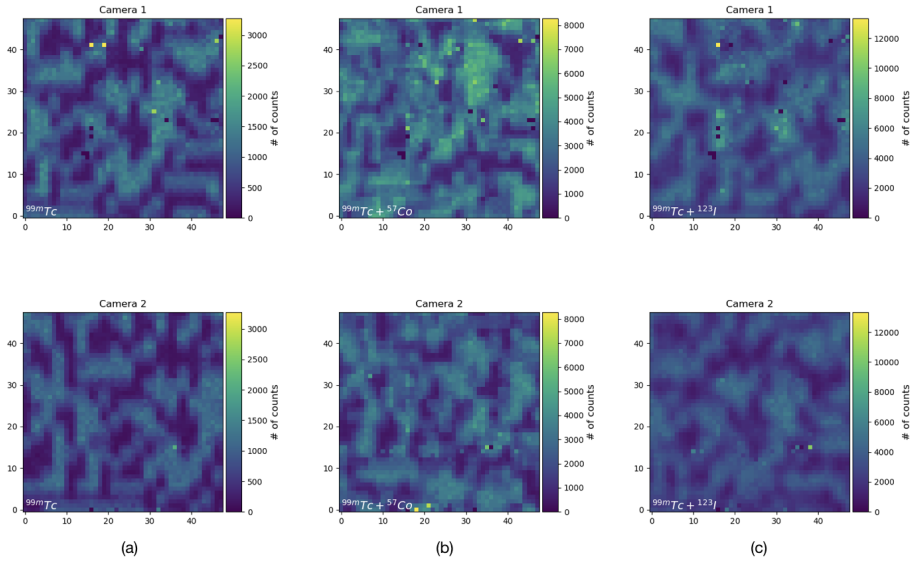

Figure 4: Detector images for point sources in 3 different configurations. (a) Single ^{99m}Tc point source. (b) ^{99m}Tc and ^{57}Co point sources. (c) ^{99m}Tc and ^{123}I point sources.

Peak parameters

	position (x mm, y mm, z mm)	peak value (AU)	SNR
Source A raw image	(-30, -30, -30)	446568	21.5
Source B raw image	(30, 30, 30)	160842	7.8
Source A cleaned image	(-30, -30, -30)	443887	186.1
Source B cleaned image	(30, 30, 30)	144560	60.6

Table 1: Brightness, location and SNR of sources in the reconstructed images. Coordinates are in mm, in a frame of reference with origin in the the centre of the FOV, x-y plane parallel to the detector plane of camera 1, and z axis orthogonal to it.

4. EXPERIMENTAL DATA

The imaging system was tested with different types of sources in the laboratories of the Nuclear Medicine Departments of the Royal Surrey County Hospital and the Southampton General Hospital. The tests involved single and pairs of point sources, a single extended source, and a hollow sphere phantom. Energy cuts were applied to the data to isolate the photopeak of each isotope. The energy windows of the selected events were 118 keV to 124 keV for ^{57}Co, 137 keV to 144 keV for ^{99m}Tc and 155 keV to 162 keV for ^{123}I. Different isotopes were used to test the potential of the imaging system to separate and identify different sources.

4.1 Point sources

The point sources imaged during the tests were of three different isotopes, ^{57}Co, ^{99m}Tc and ^{123}I. ^{57}Co is a commercially available spot marker, ^{99m}Tc and ^{123}I are obtained by filling the tip of a 10 ml syringe with the isotope in solution. Three images of point sources were collected: the single ^{99m}Tc point source, ^{99m}Tc with ^{57}Co, and ^{99m}Tc with ^{123}I. The shadowgrams of these acquisitions are shown in figure 4 and the details of each acquisition are summarised in table 2.

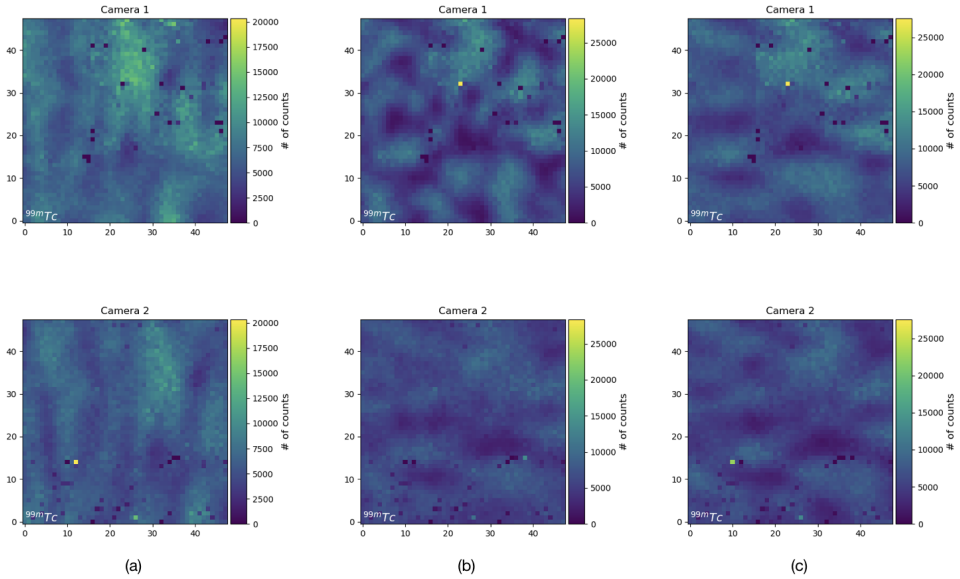

Figure 5: Shadowgrams the ^{99m}Tc cylindrical source in 3 different configurations. (a) Vertical. (b) Parallel to the axis of camera 1 (c) at a 45 degrees angle to both camera axes. In each configuration, the source was placed at the centre of the FOV.

4.2 Extended source

An extended source, pictured in figure 6, was prepared by filling a 5 ml syringe with a ^{99m}Tc solution. The source has a cylindrical shape with a base diameter of 12 mm and a height of 25 mm. Figure 5 shows the shadowgrams obtained by scanning the syringe in three different configurations: standing vertically, horizontally with the axis parallel to the axis of camera 1, and horizontally at an angle of 45 degrees to both camera axes. The details of

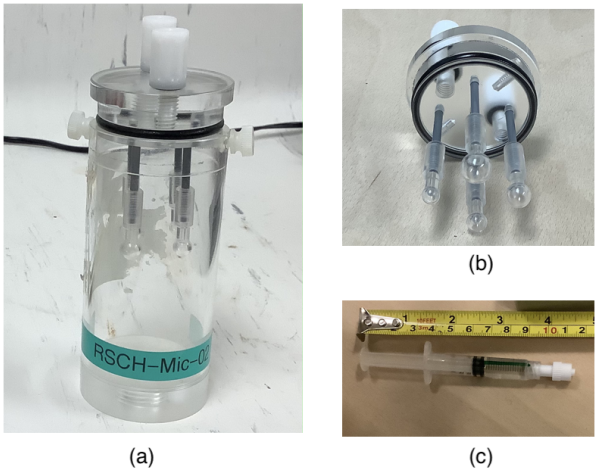

Figure 6: The extended sources used in the experiments. (a) The hollow sphere phantom. (b) The sphere components of the hollow sphere phantom. (c) A 5 ml syringe full of ^{99m}Tc solution (cylindrical source).

the acquisition are shown in table 3. Although the mask pattern is not clearly recognisable, the orientation of the source relatively to each camera appears in the features in each shadowgram.

4.3 Hollow sphere phantom

The hollow sphere phantom shown in figure 6 is an ∼8.2 cm cylindrical phantom with a base of ∼4cm diameter. Four hollow spheres of diameter 3.95 mm, 4.95 mm, 6.23 mm and 7.86 mm can be placed inside the cylinder, approximately 1.3 cm off the center and 5.3 cm from the lid of the cylinder. The spheres were filled with a ^{123}I solution, and the background consisted of a ^{99m}Tc solution. The phantom was scanned at the centre of the FOV. The shadowgrams and the spectrum of the phantom are displayed in figure 7.

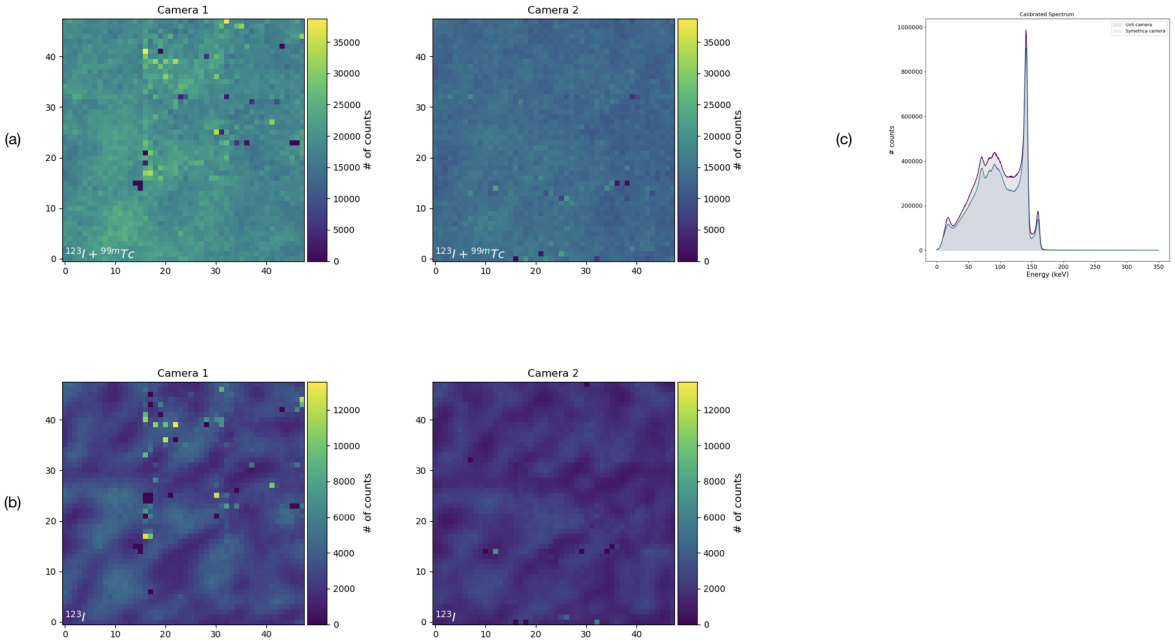

Figure 7: (a) Shadowgrams of the hollow sphere phantom in the energy windows 137 - 144 keV and 155 -162 keV. (b) Shadowgrams of the hollow sphere phantom in the energy window 155 -162 keV. (c) Spectra of the emission from the phantom recorded by both detectors.

Table 2: .

Isotope	Activity (MBq)	Intensity(AU)	Acquisition time (s)	Detector flux (cts s^{-1} cm^2)	
				Detector 1	Detector 2
^{99m}Tc	0.82	$9.27 \cdot 10^5$	3600	21.59	21.45
^{99m}Tc	0.19	$1.99 \cdot 10^6$	21600	10.98	10.92
^{57}Co	0.02	$1.88 \cdot 10^6$			
^{99m}Tc	8.03	$1.98 \cdot 10^6$	2700	118.91	114.43
^{123}I	6.5	$1.08 \cdot 10^6$			

5. RESULTS

In this section 3D images obtained from the shadowgrams with a back-projection reconstruction are shown before and after the application of different numbers of iterations of the CLEAN algorithm with a 2% gain.

Table 3: Sources, activity and acquisition times of extended source scans.

Source	Isotope	Activity(MBq)	Acquisition time (s)	Detector flux (cts s^{-1} cm^2)	
				Detector 1	Detector 2
Cylinder (vertical)	^{99m}Tc	34.46	900	643.33	628.07
Cylinder (horizontal)	^{99m}Tc	32.69	900	640.39	652.07
Cylinder (horizontal 2)	^{99m}Tc	30.92	900	674.93	625.65
Hollow spheres phantom	^{123}I ^{99m}Tc	16.11 71.96	3600	628.82	539.53

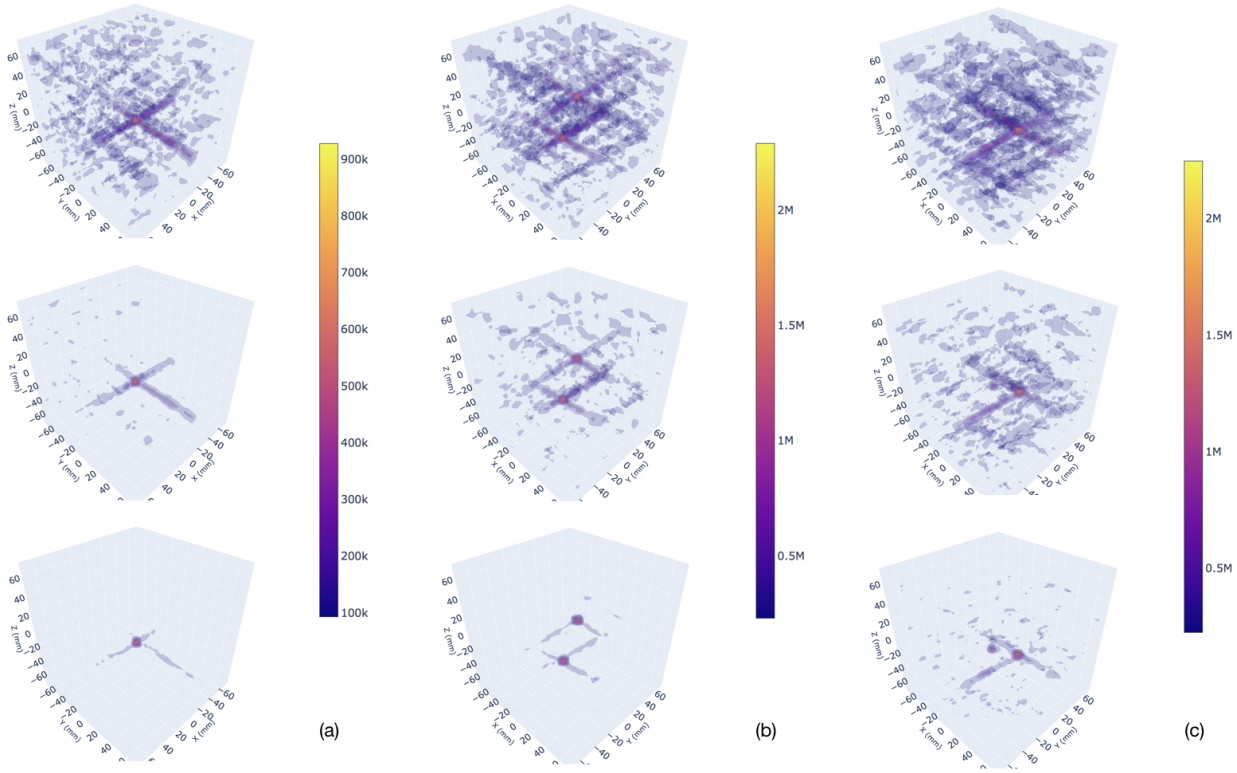

Figure 8: (a) Images of a single point source of ^{99m}Tc (b) Image of ^{57}Co and a ^{99m}Tc point sources. (c) Image of ^{99m}Tc and a ^{123}I. In each case, the graphs display the raw image at the top, the cleaned image after 50 CLEAN iterations at the centre and after 300 CLEAN iterations at the bottom.

5.1 Point Sources

Single or multiple point sources represent an ideal scenario for the best performance of both coded apertures and CLEAN. The technique performed very similarly to what was predicted by the simulations in both cases. Figure 8 shows the raw images of all three point source configurations, along with the images after 50 and 300 CLEAN iterations. If only one source is present in the FOV, most of the background noise is suppressed after 50 iterations. The advantage of using a dual-head system is visible. The features extending from the central hot region of the image are residuals from the elongated PSF of a single camera. The addition of the second camera constrains the position of the point source. Adding a second source to the FOV makes CLEAN slower: after 50 iterations there is still a considerable amount of noise. In fact CLEAN will operate on both sources, subtracting components from one of them in each loop. In figure 8(c) it is shown that the ^{123}I point source is not clearly

visible, and becomes distinguishable from the noise only after iteration 300. The relative intensity of the source is conserved after the application of CLEAN and correctly corresponds to the detector flux.

5.2 Hollow sphere phantom

The raw image of the hollow sphere phantom in the energy range $137-144$keV is displayed in figure 9(a). Images 9(b) and 9(c) show the same image after 100 and 500 iterations of CLEAN respectively. While only the three bigger spheres were distinguishable in the raw image, applying CLEAN made the smaller sphere distinguishable from the background in the cleaned image.

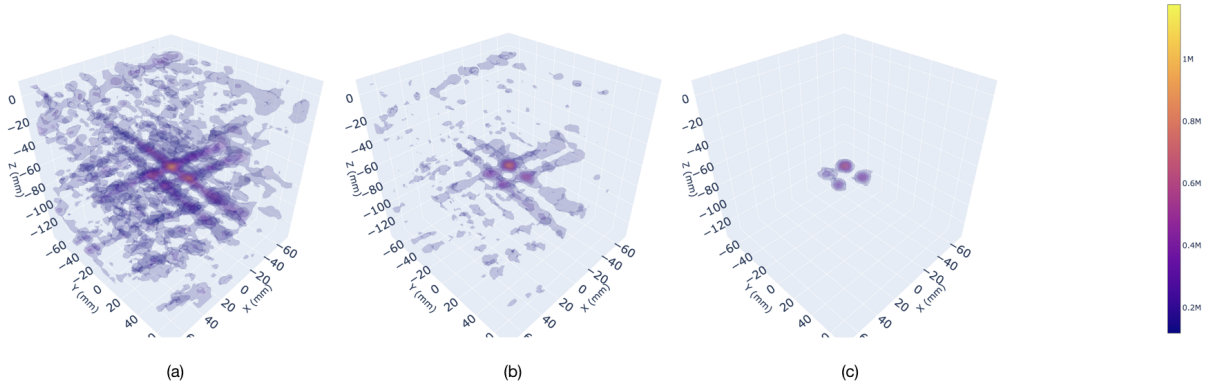

Figure 9: (a)Raw image of the hollow spheres phantom. (b) Image of the hollow spheres phantom after 100 CLEAN iterations. (c)Image of the hollow spheres phantom after 300 CLEAN iterations.

5.3 Extended source

Figure 10(c) displays the 3D images of the cylindrical sources after 500 CLEAN iterations. The shape of the extended source is clearly recognisable only in figure 10(a). This suggests that the deconvolution algorithm is not as effective in the reconstruction of sources that extend along one of the axes of the camera, which happens in the configurations in figures 10(b) and 10(c).

6. CONCLUSIONS

The images obtained by the application of a back-projection reconstruction and CLEAN show the best results on point source imaging, with the most dramatic increase in the SNR with respect to the raw image. The image quality decreases for more extended sources, especially if they extend in the direction of one of the cameras axis, along which the raw resolution is poor. This was expected, since coded apertures with very high transmission are known to perform better for concentrated sources. When a source occupies a significant fraction of the FOV, the emission is so distributed that the deconvolution recovers the information on the source configuration only partially. In fact the information on the source morphology is encoded in the shadowgram as the contrast between brighter and darker pixels, which is worse as the size of the source increases, as can be noted from comparing the shadowgrams in figures 4 and 7. The application of CLEAN still provides an improvement, though not as pronounced as in the point source images. These characteristics and the instrument capability of separating isotopes indicate parathyroid imaging as one of the most appropriate applications of this technique. Multi-isotope imaging with ^{99m}Tc and ^{123}I could guide and aide parathyroid excision, distinguishing between thyroid and parathyroid glands. Accorsi[4] carried out an extensive studies of the SNR properties of coded aperture imagers in different source and mask configurations, concluding that the camera design should be tailored to the specific medical application to obtain optimal image quality. Maximum likelihood expectation maximization (MLEM) has also proven to perform very well in terms of background suppression in the image decoding and will also be applied to the imaging system described here as a future development of this project.

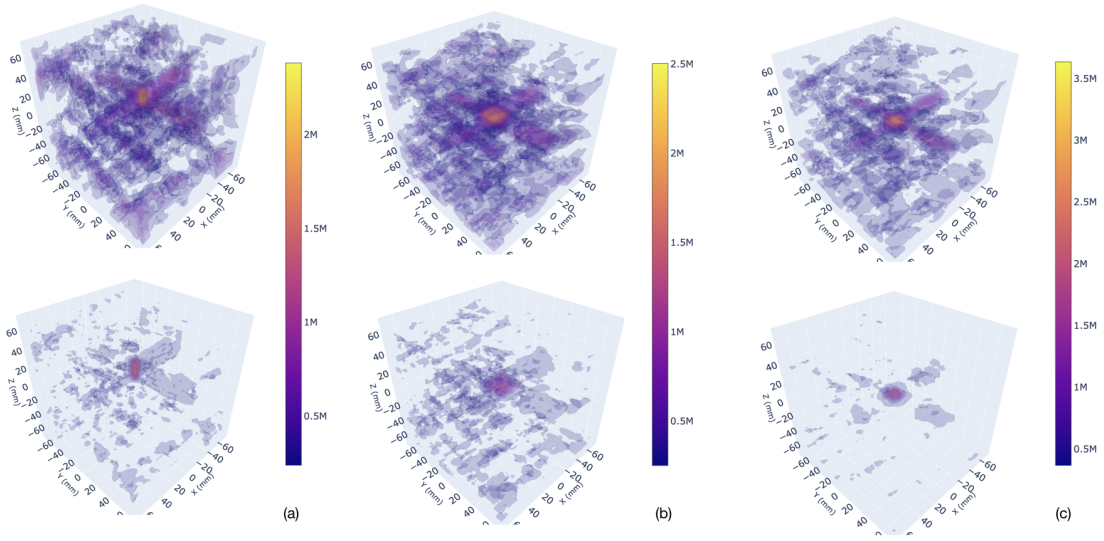

Figure 10: Images of the cylindrical source in configuration 1 (a), configuration 2 (b) and configuration 3 (c). The raw images are shown at the top, while the images processed with CLEAN after 500 iterations are at bottom.

7. ACKNOWLEDGEMENTS

We would like to thank the Southampton company Symetrica for the loan of one of the camera heads and especially Ian Della-Rocca, who has designed the data acquisition software used in the experiments. This work would not have been possible without the resources from the Nuclear Medicine departments of the Royal Surrey County Hospital and the Southampton General Hospital. We are really grateful for the support from both institutions. We would like to offer our special thanks to Gemma Lewis and Timothy Melhuish for preparing the samples during the experimental phase of the project at Southampton General Hospital.

REFERENCES

[1] Costantino, A., "Constructing an IBIS/ISGRI slew survey," in [*Proceedings of 2th Integral Conference : 1st AHEAD Gamma-ray Workshop*], 716–731 (2019).
[2] Z. Mu, Y. L., "Aperture collimation correction and maximum likelihood image reconstruction for near-field coded aperture imaging of single photon emission computerized tomography," (2006).
[3] Z. Mu, L. Dobrucki, Y. L., "Spect imaging of 2-D and 3-D distributed sources with near-field coded aperture collimation: computer simulation and real data validation," (2016).
[4] R. Accorsi, F. Gasparini, R. L., "A coded cperture for high-resolution nuclear medicine planar imaging with a conventional anger camera: experimental results," (2001).
[5] E. Fenimore, T. M. C., "Coded aperture imaging with uniformly redundant arrays," 377 (1978).
[6] Byard, K., "Application of the CLEAN algorithm to three dimensional coded aperture imaging," (2020).
[7] L. A. Shepp, Y. V., "Maximum likelihood reconstruction for emission tomography," (1982).
[8] NVIDIA, "Cuda toolkit, develop, optimize and deploy gpu-accelerated apps,"
[9] Python, "Numba: A high performance python compiler,"
[10] A. Goldwurm, P. e. a., "Gamma-ray imaging with the coded mask ibis telescope," (2001).
[11] Högbom, J., "Aperture synthesis with a non-regular distribution of interferometer baselines," (1974).
[12] G. B. Taylor, C. L. Carilli, R. A. P., "Synthesis imaging in radio astronomy ii," (1999).